

Article

Towards an Ultra-High-Speed Combustion Pyrometer[†]

Alberto Sposito, Dave Lowe and Gavin Sutton * 

National Physical Laboratory (NPL), Hampton Road, Teddington TW11 0LW, UK;
sposito.alberto@gmail.com (A.S.); dave.lowe@npl.co.uk (D.L.)

* Correspondence: gavin.sutton@npl.co.uk

† This paper was presented at the 9th EVI-GTI International Gas Turbine Instrumentation Conference, Graz, Austria on 20–21 November 2019.

Received: 2 March 2020; Accepted: 10 December 2020; Published: 15 December 2020



Abstract: Measuring reliably the correct temperature of a sooty flame in an internal combustion engine is important to optimise its efficiency; however, conventional contact thermometers, such as thermocouples, are not adequate in this context, due to drift, temperature limitation (≤ 2100 K) and slow response time (~ 10 ms). In this paper, we report on the progress towards the development of a novel ultra-high-speed combustion pyrometer, based on collection of thermal radiation via an optical fibre, traceably calibrated to the International Temperature Scale of 1990 (ITS-90) over the temperature range $T = (1073\text{--}2873)$ K, with residuals $< 1\%$, and capable of measuring at a sampling rate of 250 kHz.

Keywords: combustion; temperature; pyrometer; optical sensor

1. Introduction

Traceable, reliable measurement of combustion temperature is important because it can improve the understanding of the combustion process and provide a mechanism for the optimisation of engine power, fuel consumption and emissions [1]. These measurements are performed under highly dynamic conditions, with temperature changes of up to ~ 3300 K occurring on a millisecond timescale. Conventional temperature sensors based on contact thermometry (e.g., thermocouples) are inadequate in this context, due to their slow response time (~ 10 ms), temperature limitation (≤ 2100 K), drift and perturbation of the combustion process. To address this challenge, with particular reference to internal combustion and diesel engines, we are developing a novel ultra-high-speed combustion pyrometer, within the framework of the European joint research project DynPT—Development of measurement and calibration techniques for dynamic pressures and temperatures, part of the European Metrology Programme for Innovation and Research (EMPIR) [2].

2. System Design and Theoretical Model

A schematic of the thermometer system design is shown in Figure 1. It consists of:

- A sensor: a 2 m long gold-coated multi-mode (MM) step-index fibre, with $400\ \mu\text{m}$ core diameter, numerical aperture $NA = 0.22$, stainless-steel monocoil sheathing, a sub-miniature (SMA) connector on one end (hot front end) and a fibre-channel (FC) connector on the other end (cold back end)—for testing purposes, this was placed inside a ~ 1.7 m long stainless-steel tube (outer diameter: 20 mm, inner diameter: 16 mm), with the SMA connector protected by a recessed sapphire window; sensor and packaging can be tailored to the final application and installation requirements (e.g., addition of a collimating lens).
- An extension lead fibre: a lightly-armoured 10 m long MM step-index fibre patch-cord, with $600\ \mu\text{m}$ core diameter, $NA = 0.22$, dual acrylate coating, 3 mm diameter polyvinyl chloride (PVC) sleeve and FC connectors on both ends—this connects the sensor (on the FC connector) to the interrogator.

- A passive optoelectronic interrogator, assembled in-house and consisting mainly of:
 - a custom-made $1 \times 3 \text{ mm}^2$ step-index fibre coupler/splitter with $600 \mu\text{m}$ core diameter, $NA = 0.22$ and FC connectors on all ports;
 - three photodetector assemblies, using off-the-shelf components, for measuring optical thermal radiation at 3 different wavelengths: $\lambda_1 = 850 \text{ nm}$, $\lambda_2 = 1050 \text{ nm}$ and $\lambda_3 = 1300 \text{ nm}$;
 - a power supply unit to power the photodetectors.
- A National Instrument (NI) data acquisition (DAQ) system, with maximum sampling rate $f_{MAX} = 1 \text{ MHz}$, connected to the optoelectronic interrogator via BNC cables and to a Personal Computer (PC) via a USB cable.

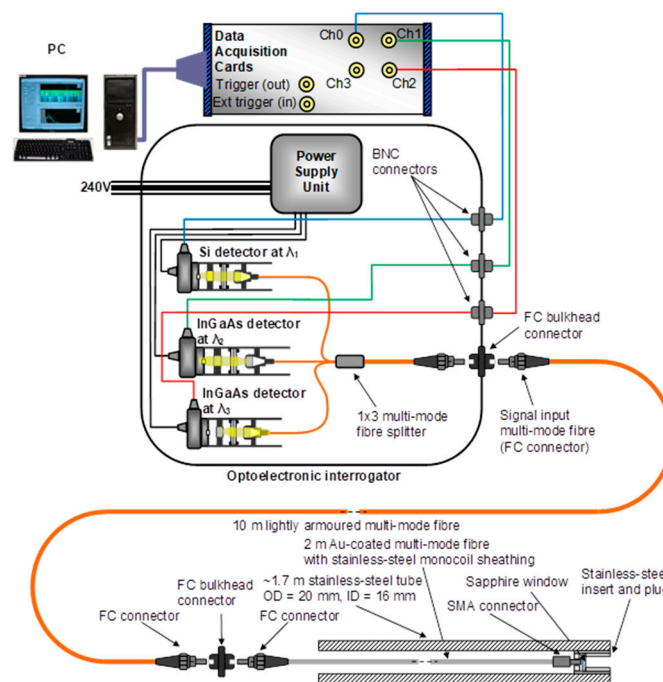


Figure 1. Schematic of the system.

Fibres with large core diameter and large NA were chosen to maximise collection of optical thermal radiation; the gold (Au) coating allows the fibre to withstand high temperatures, up to $\sim 1000 \text{ K}$, although the core diameter of Au-coated fibres is limited to $400 \mu\text{m}$.

The wavelengths of the photodetector assemblies were chosen based on previous experience to avoid spectral features (emission and absorption lines) from the combustion by-products and the components of the pyrotechnic charges (see figures below, taken from earlier spectroscopic experiments), as well as to test the assumption that the measured combustion process behaves like a blackbody (emissivity $\varepsilon = 1.0$)—good agreement amongst the temperatures estimated at different wavelengths can be used to confirm that the blackbody condition is met.

Figure 2a shows the emission spectrum captured with a Si spectrometer, where the following features were identified:

- A. 589 nm—Sodium (Na) emission lines;
- B. 619 nm—CaOH emission lines;
- C. 693 nm—Potassium (K) emission lines;
- D. 767 nm—K emission and absorption lines;
- E. 960 nm—Uncertain of assignment.

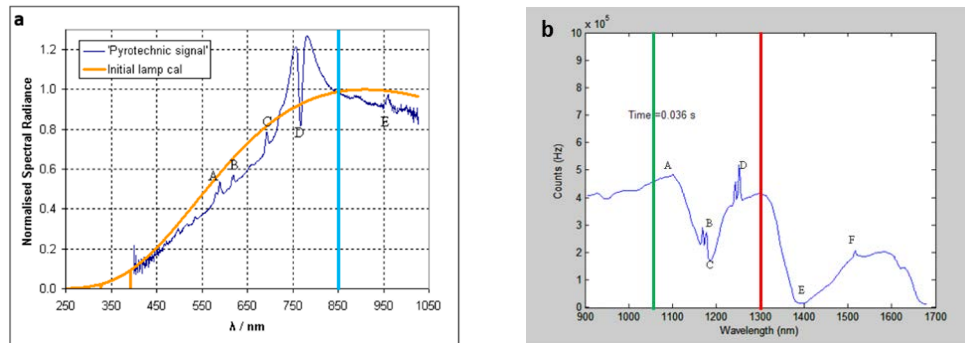


Figure 2. Pyrotechnic emission spectrum from (a) Si spectrometer, (b) InGaAs spectrometer, ~36 ms after ignition. The coloured vertical lines identify the chosen wavelength: 850 (blue line in (a)), 1050 (green line in (b)) and 1300 nm (red line in (b)).

Figure 2a also shows the blackbody spectrum from a tungsten calibration lamp (with a temperature of 3165 K) overlapped to the measured spectrum. The agreement between the shape of the two spectra suggests that the blackbody assumption for a fireball is a valid hypothesis.

Figure 2b shows the emission spectrum captured with an InGaAs spectrometer, where the following features were identified:

- A. 1104 nm—K emission lines;
- B. 1169 nm—K emission lines;
- C. Broad OH absorption in the fibre;
- D. 1243 and 1252 nm—K emission lines;
- E. Broad OH absorption in the fibre;
- F. 1517 nm—K emission lines.

As photodetectors with variable gain G were used, a simple theoretical model was developed to estimate the optical power measured by each photodetector and how their voltage signals change with G . Their bandwidth B also decreases with increasing G , adjustable in 10 dB steps from 0 to 70 dB.

First of all, the blackbody radiation power coupled into the core of the optical fibre (see geometry sketched in Figure 3) was calculated, assuming an emissivity $\epsilon = 1$ and optical transmission of the fibre over the range $\lambda = (0.3\text{--}2.4) \mu\text{m}$ as specified in the Au-coated fibre datasheet.



Figure 3. Geometry of the end of the sensor (Au-coated fibre): d = fibre core diameter; θ = maximum acceptance half-angle.

Neglecting the Fresnel reflection losses from the end-facet of the fibre and from the sapphire window, the total blackbody radiation power coupled into the fibre core over the full blackbody radiation spectrum (i.e., all wavelengths) is:

$$P_{in, TOT}(T) = \Omega A \varepsilon \sigma T^4 / \pi$$

where:

- T is the blackbody temperature in K;
- $\sigma = 5.67 \times 10^{-8} \text{ W} \cdot \text{m}^{-2} \cdot \text{K}^{-4}$ is the Stefan–Boltzmann constant;
- $A = \pi d^2/4 = 1.25664 \times 10^{-7} \text{ m}^2$ is the fibre core area;
- $\Omega = \pi \tan^2(\theta)$ is the maximum solid acceptance angle of the Au-coated fibre, with θ the maximum acceptance half-angle of the Au-coated fibre, which is related to the NA of the fibre as: $NA = n \sin(\theta) = 0.22$

As the refractive index of air is $n \approx 1$, the maximum solid acceptance angle can be re-written as:

$$\Omega = \pi \tan^2(\arcsin(NA)) \approx 0.16 \text{ sr}$$

Hence, the total blackbody radiation power coupled into the optical fibre is:

$$P_{in, TOT}(T) \approx 3.624 \times 10^{-16} T^4 \text{ W}$$

The fractional power coupled into the optical fibre over the wavelength range $\lambda = (0.3\text{--}2.4) \mu\text{m}$, $P_{in}(T)$, can be calculated numerically or through tabulated values, considering the wavelength-temperature products.

With such a model, approximately 10 mW of optical thermal radiation is coupled into the optical fibre for $T \approx 2500 \text{ K}$; however, for $T = 300 \text{ K}$: $P_{in}(T) < 10 \text{ pW}$.

To calculate the optical power measured by each photodetector and the associated voltage signals, the losses in the optical transmission line from the sensor head to the detectors need to be considered. To estimate the signals accurately, the following contributions need to be taken into account:

1. The transmission factor of the sapphire window placed in front of the fibre end-facet, due to Fresnel reflection losses (7% at each interface/surface): $t_0 = 0.93 \times 0.93 = 0.8649$.
2. The transmission factor at the end-facet of the Au-coated fibre, due to Fresnel reflection losses: $t_1 = 0.96$.
3. Transmission losses of 12 m of fibre (2 m sensor + 10 m of extension lead fibre)—considering that typical losses for large-core multi-mode fibre are of the order of 10 dB/km or less at $\lambda = (0.6\text{--}1.6) \mu\text{m}$: $t_{\text{fibre}} = -0.12 \text{ dB} \approx 0.973$.
4. Losses due to optical connectors (3), typically of the order of 0.3 dB each—i.e., a transmission factor $t_{\text{connector}} = 0.933$
5. The splitting ratio of the 1×3 optical coupler/splitter: $t_{\text{splitter}} \approx 0.333$.
6. The optical transmission (t_{filter}) of the bandpass filters in the photodetector assemblies—it is worth noting that the filters used have different values of optical transmission peak and Full-Width-at-Half Maximum (FWHM):
 - $t_{850 \text{ nm}} = 70\%$;
 - $t_{1050 \text{ nm}} = 45\%$;
 - $t_{1300 \text{ nm}} = 40\%$;
 - $\text{FWHM}_{850 \text{ nm}} = 40 \text{ nm} \pm 8 \text{ nm}$;
 - $\text{FWHM}_{1050 \text{ nm}} = 10 \text{ nm} \pm 2 \text{ nm}$;
 - $\text{FWHM}_{1300 \text{ nm}} = 30 \text{ nm} \pm 6 \text{ nm}$.

Hence, the optical power incident on the photodetectors can be calculated as:

$$P_i(\lambda, T) = t_0 t_1 t_{\text{fibre}} t_{\text{splitter}} (t_{\text{connector}})^3 t_{\text{filter}}(\lambda) P_{in}(\lambda, T) \approx 0.22 t_{\text{filter}}(\lambda) P_{in}(\lambda, T) \quad (1)$$

Finally, to calculate the voltage signal, we also need to consider the photodetector transimpedance gain G_i [V/A] and responsivity $R(\lambda_i)$ [A/W], which is a function of wavelength; hence:

$$V_i = \int G_i R_i(\lambda) P_i(\lambda, T) d\lambda = 0.22 G_i \int t_{\text{filter}}(\lambda) R_i(\lambda) P_{in}(\lambda, T) d\lambda \quad (2)$$

where:

$$P_{in}(\lambda, T) = A \Omega L_b(\lambda, T)$$

with:

$$L_b(\lambda, T) = \frac{2c_1}{\lambda^5} \frac{1}{e^{c_2/\lambda T} - 1} \approx \frac{2c_1}{\lambda^5} e^{-c_2/\lambda T}$$

where c_1 and c_2 are the first and second radiation constants equal to $0.59552197 \times 10^{-16} \text{ W}\cdot\text{m}^{-2}\cdot\text{sr}^{-1}$ and $1.438769 \times 10^{-2} \text{ m}\cdot\text{K}$, respectively, and the expression after the \approx symbol is the Wien approximation valid for $c_2 \gg \lambda T$.

Equations (1) and (2) were evaluated at different temperatures, with the results compared with preliminary experimental data. These showed a lower signal than expected (by a factor of ~ 2), likely due to extra connection losses. This was fed back into the model, which gave the results shown in Figure 4 in terms of optical power incident onto the photodetectors—noise floors are shown only for: $G = 0 \text{ dB}$, $B = 12 \text{ MHz}$ (highest noise floor); $G = 20 \text{ dB}$, $B = 1 \text{ MHz}$ and $G = 70 \text{ dB}$, $B = 3 \text{ kHz}$ (lowest noise floor).

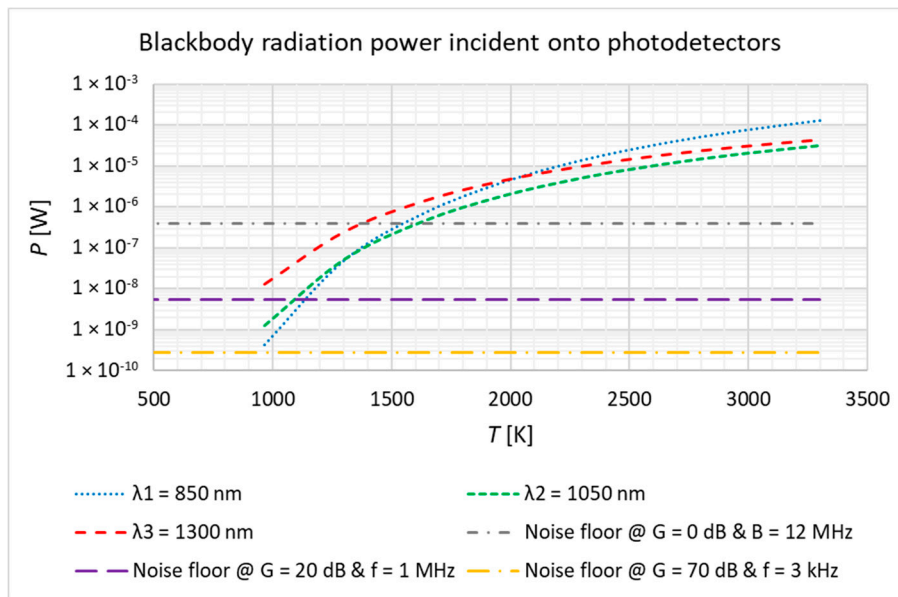


Figure 4. Blackbody radiation power incident onto photodetectors as a function of blackbody temperature.

Noise floor was estimated for each photodetector as:

$$P_{n,i} = NEP \times B^{1/2} \times R_{MAX} / R(\lambda_i)$$

where NEP is the Noise Equivalent Power and R_{MAX} is the peak responsivity—both provided in the photodetector datasheets.

Figure 4 shows that, in any case, the instrument should be capable of measuring temperatures $T > 1600 \text{ K}$ at all wavelengths, with photodetectors set at $G = 0 \text{ dB}$ and $B = 12 \text{ MHz}$. However, considering that the maximum sampling rate of the DAQ system is $f_{MAX} = 1 \text{ MHz}$, a gain setting of

$G = 20$ dB ($B = 1$ MHz) would allow measurement of temperatures as low as ~ 1000 K with the 1300 nm photodetector (but not at $\lambda_1 = 850$ nm and $\lambda_2 = 1050$ nm), with no penalty in terms of speed.

The minimum and maximum temperatures measurable by the instrument are dictated, respectively, by the noise level (experimentally measured as ~ 1 mV for most values of G) and the saturation level (~ 10 V) of the photodetectors. To find the photodetector settings that optimise the measurable temperature range, Equation (2) was evaluated at different temperatures for different G and B settings of the photodetectors. Voltage signals generated by the three photodetectors were plotted versus temperature for all values of G and B . Figure 5 shows two of these plots for representative values of G and B .

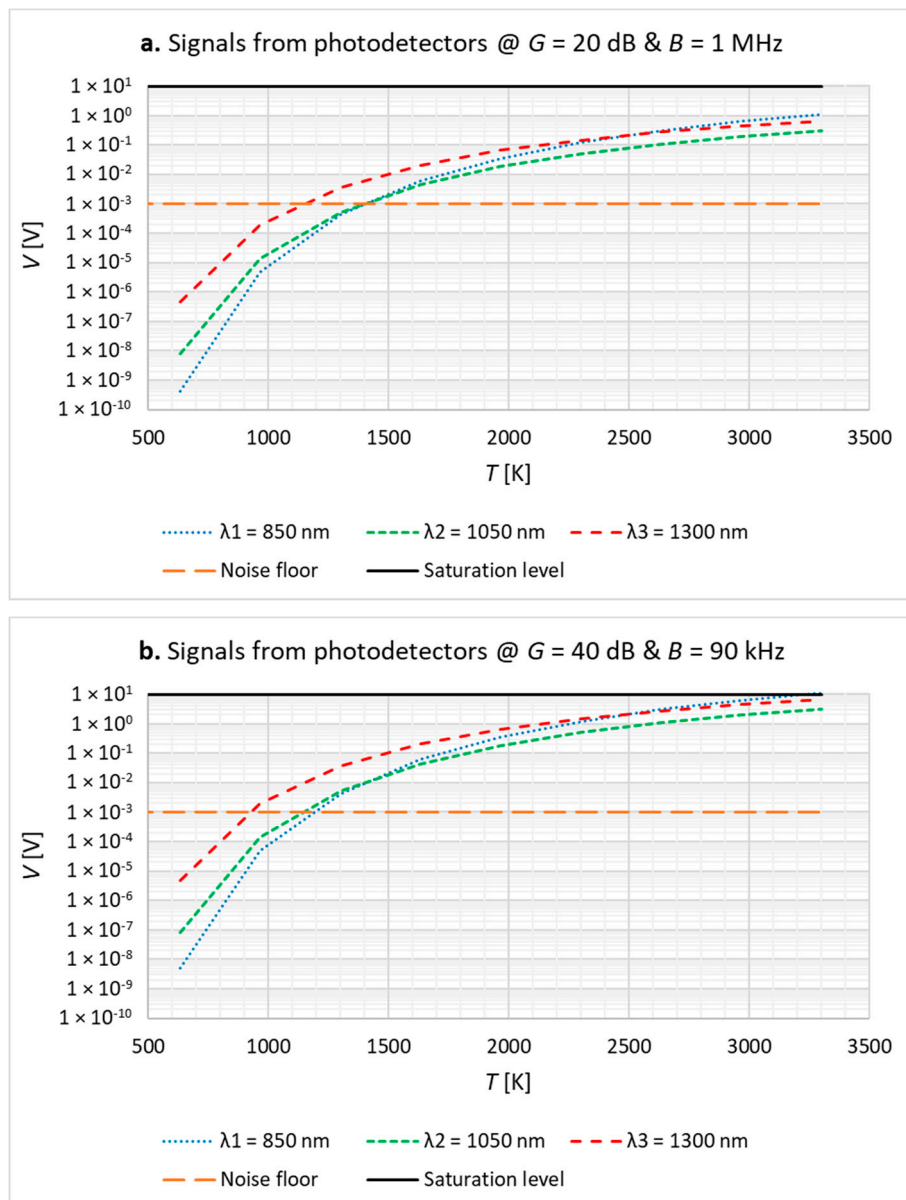


Figure 5. Modelled signals from photodetectors versus blackbody temperature at different G and B settings: (a) $G = 20$ dB and $B = 1$ MHz, (b) $G = 40$ dB and $B = 90$ kHz.

- With a gain of $G = 20$ dB ($B = 1$ MHz—Figure 5a), the instrument can measure a minimum temperature of ~ 1150 K at a single wavelength ($\lambda_3 = 1300$ nm) or ~ 1400 K at all three wavelengths.
- With a gain of $G = 30$ dB ($B = 260$ kHz), the minimum measurable temperature can be brought down to ~ 1025 K for single-wavelength measurement ($\lambda_3 = 1300$ nm) and ~ 1275 K at all three

wavelengths, but at cost of reduced sampling speed ($f \leq B = 260$ kHz), while still avoiding saturation at 3300 K, our maximum temperature of interest.

- With a gain of $G \geq 40$ dB ($B = 90$ kHz—Figure 5b), the photodetectors would start saturating at $T_{MAX} < 3300$ K and their bandwidth would decrease significantly, down to $B = 3$ kHz at $G = 70$ dB.

Hence, the optimum photodetector gain is $G = 30$ dB, which allows temperatures above 1025 K to be measured for $\lambda_3 = 1300$ nm, or temperatures above 1275 K to be measured for all wavelengths, with a maximum sampling rate $f \leq B = 260$ kHz.

3. Instrument Calibration

3.1. Test Rig

The instrument was calibrated using a Thermo Gauge blackbody radiation furnace and a KE-Technologie GmbH LP3 linear pyrometer calibrated traceably to the ITS-90 [3], with the stainless-steel tube of the packaged sensor filled with sand to avoid overheating the Au-coated fibre that could be irreversibly damaged. A photograph of part of the test rig is shown in Figure 6: the hot Thermo Gauge blackbody furnace and temperature sensor are visible in the background and foreground, respectively. The latter is placed on a stainless-steel V-groove mounted on an optical breadboard and safely held in place by removable brackets bolted to the breadboard. This breadboard is installed on a motorised stage, controlled by a computer, for horizontal and vertical alignment. The LP3 (not visible in Figure 6) is mounted on the same framework, so that it can be easily moved in front of the blackbody, in place of the sensor, to measure the temperature at each setpoint of the calibration.

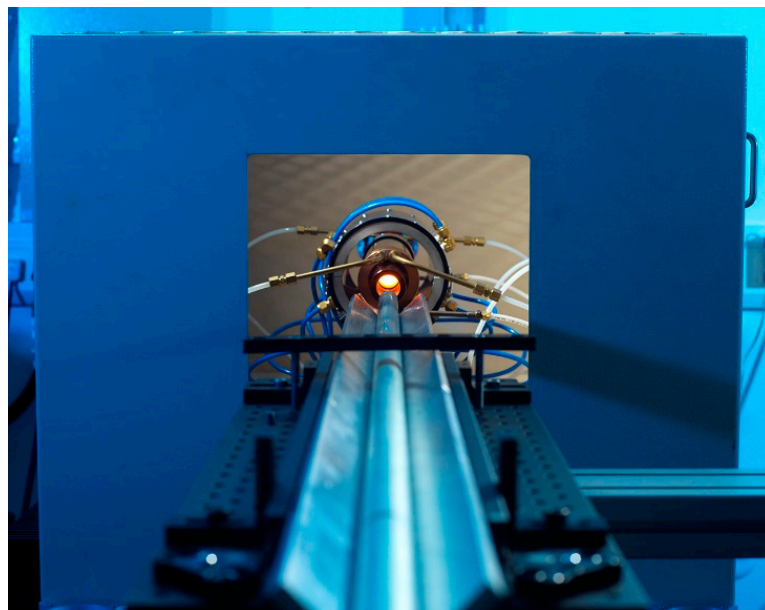


Figure 6. Photograph of the calibration furnace: the instrument sensor, housed in a steel tube, is sitting on the V-groove placed in front of blackbody furnace, ready to be manually moved in and out of it for dynamic calibration at a set temperature.

Data from the instrument were acquired using a NI LabVIEW program written in-house and executed on the PC that is part of the system, whereas the blackbody furnace was controlled with a separate desktop computer that also controls the motorised framework.

3.2. Test Method

The instrument was configured with the photodetectors set with optimum gain $G = 30$ dB ($B = 260$ kHz) and the sampling rate set at $f = 250$ kHz. At the beginning of the calibration, the voltage offset from the three photodetectors was measured once, to zero the photodetectors.

The instrument was calibrated in the temperature range $T = (1073\text{--}2873)$ K, in steps of $\Delta T = 200$ K, according to the following procedure:

1. The blackbody furnace was set at the required temperature set-point.
2. The temperature of the blackbody cavity was monitored using the LP3.
3. Once the blackbody temperature reached stability, a measurement was taken from the LP3, by measuring the average and standard deviation over ~ 30 s (the LP3 is sampled at 1 Hz).
4. The LP3 was moved out of the way and the sensor moved into place, so that it was in line with and parallel to the long axis of the blackbody, as shown in Figure 6.
5. Data acquisition and logging were started on the instrument.
6. Manually, the sensor was quickly moved into and out of the blackbody (within a few seconds).
7. Two measurements were made at each set-point temperature.

3.3. Test Data Analysis Method

The raw voltage signals from the three photodetectors of the optoelectronic interrogator were analysed to find the optimum calibration point in each signal. This is explained in Figure 7, showing typical measurement traces—the signal from the 1050 nm photodetector was the lowest, because of the combined effect of the responsivity of the photodetector and the transmission and the bandwidth of the optical bandpass filter.

Considering Figure 7b:

- $t < 1.3$ s: the blackbody cavity had a temperature gradient along the cavity wall and across its rear surface, it was hotter to the outside, and this was seen as the sensor approached: the radiance signal increased as the field of view of the sensor was initially filled.
- $t \approx (1.3\text{--}1.6)$ s: the signal fell as the sensor progressively saw more of the cooler central section of the back wall.
- $t \approx (1.6\text{--}1.77)$ s: there was a period when the blackbody temperature fell due to heat lost to the cold sensor.
- $t \approx (1.77\text{--}1.92)$ s: as the sensor was withdrawn, the hotter regions of the blackbody cavity were seen again, so that the signal increased.
- $t > 1.92$ s: the signal decreased, as the sensor was withdrawn from the blackbody cavity.
- The maximum in the signal during sensor removal was lower than during insertion. This is consistent with the cooling of the blackbody cavity.
- The voltages recorded for calibration were chosen at the inflection point of each signal, highlighted by the blue circle, as it corresponds to the point when the field of view of the fibre is filled with thermal radiation from the back wall, before any further cooling caused by the sensor.

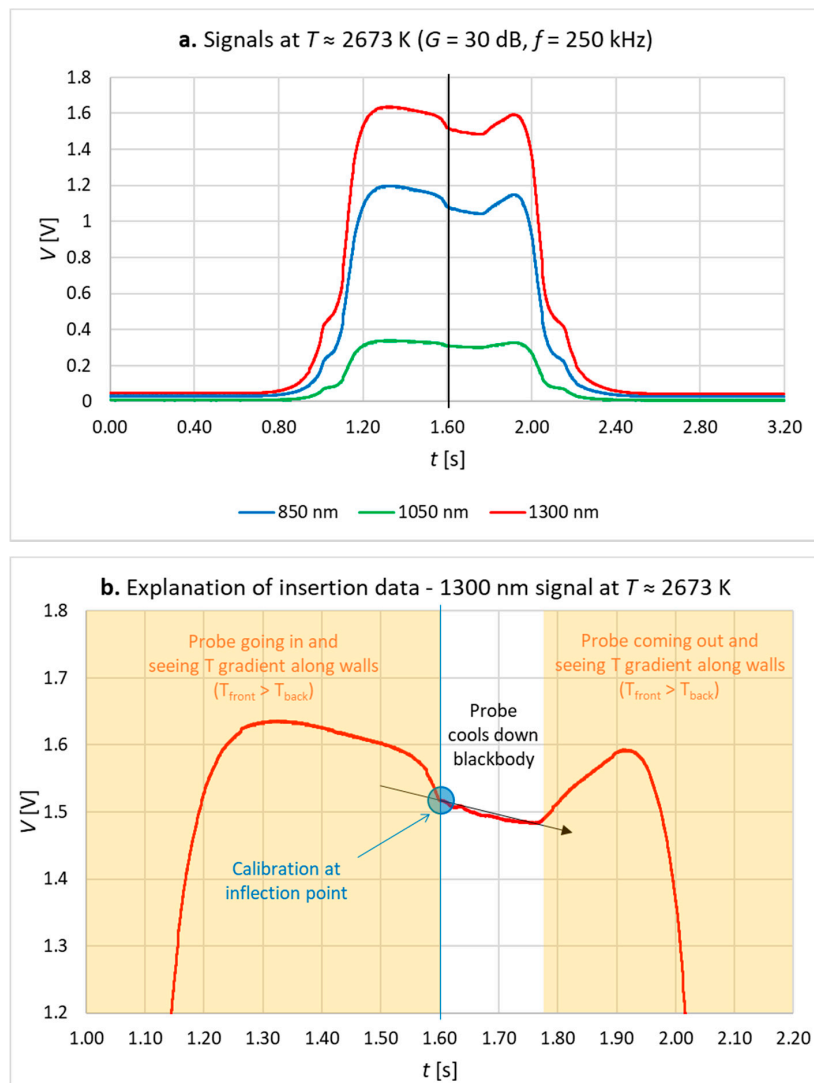


Figure 7. Typical calibration measurement traces: the black line in the middle of chart (a) identifies the points used for calibration; (b) is a close-up on the 1300 nm signal and its calibration point.

Calibration was performed by fitting experimental data to the Planckian version of the Sakuma–Hattori equation with three adjustable parameters A_i , B_i and c_i for each wavelength λ_i [4]:

$$V_i = \frac{A_i}{e^{c_i/(\lambda_i T + B_i)} - 1} \tag{3}$$

At each calibration point, the two voltage measurements for each wavelength/photodetector were averaged; each average was then converted into temperature using the inverse function of Equation (3):

$$T_i = \frac{c_i}{\lambda_i \ln\left(\frac{A_i}{V_i} + 1\right)} \tag{4}$$

Optimum values of the adjustable parameters were found using the Generalized Reduced Gradient (GRG) solving method for smooth non-linear problems, to minimise the sum of the squares of temperature differences with the LP3.

3.4. Calibration Test Results

The average signal at each setpoint was measured for each wavelength/photodetector and plotted versus the set-point temperature measured from the LP3 linear pyrometer. Figure 8 shows good agreement between experimental data and the theoretical model at $G = 30$ dB, as used for the calibration, with the signal from the 1300 nm photodetector higher than predicted, most likely due to overestimated losses, as a single figure was used for all three wavelengths. Figure 8 also shows that the instrument can measure a temperature as low as 1073 K at $\lambda_3 = 1300$ nm or 1273 K at all three wavelengths—these minimum temperatures match with those expected from the theoretical model.

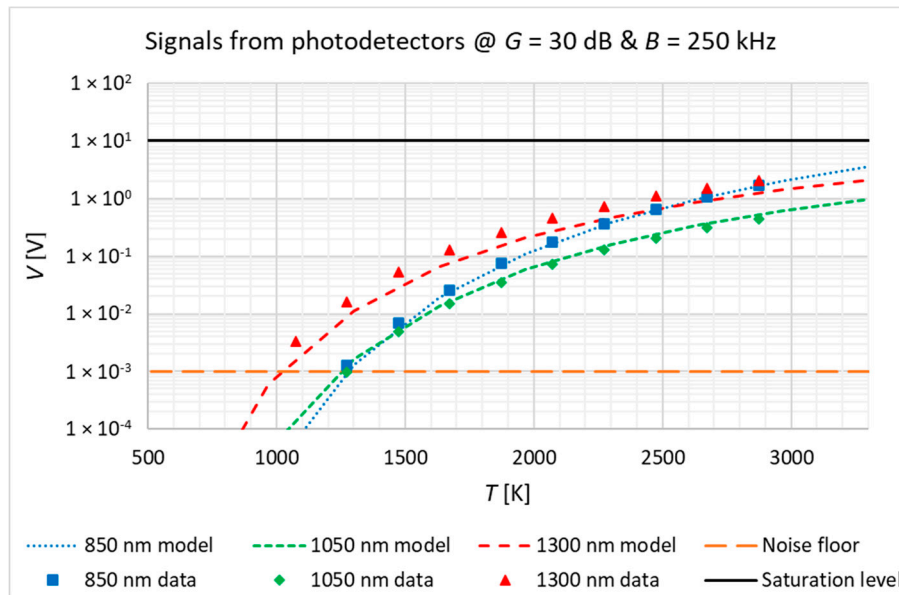


Figure 8. Experimental data compared with theoretical model.

Using the inverse Planck function—i.e. Equation (4)—average voltage measurements for each wavelength at each set-point were converted into temperatures and the adjustable parameters were optimised to minimise the sum of the squares of calibration residuals. The optimum calibration coefficients are shown in Table 1 (B_i coefficients are not included, because they were found to be equal to zero) and the residuals are shown in Figure 9, showing relative temperature differences within $\pm 1\%$ (absolute differences are within ± 15 K).

Table 1. Optimum values of the adjustable calibration coefficients, minimising sum of squares of relative errors.

λ_i [nm]	A_i [V]	c_i [$\mu\text{m K}$]
850	527.6	14,082.2
1050	53.0	14,431.8
1300	91.7	14,307.3

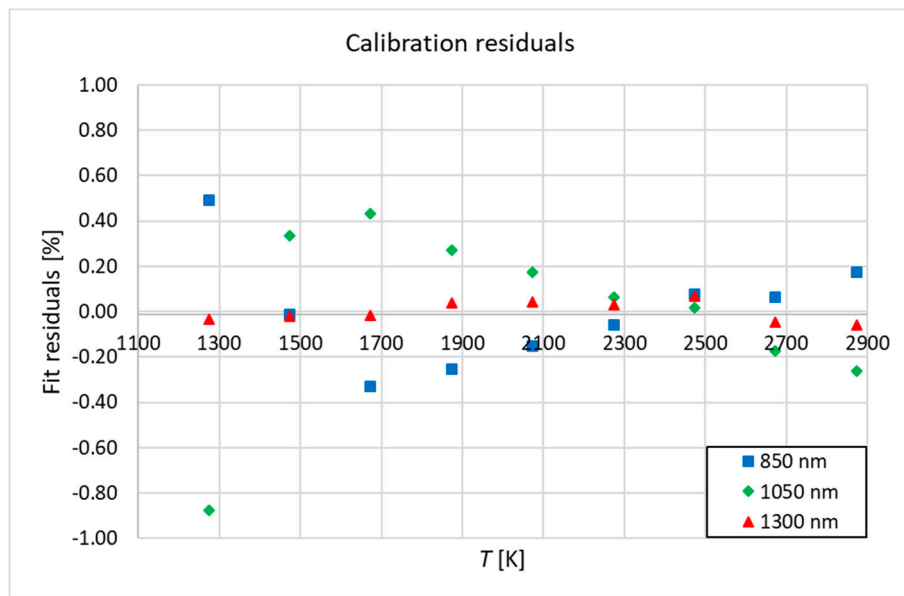


Figure 9. Calibration residuals.

Having calibrated the sensor, the maximum measurable temperatures can be estimated by extrapolation of the Planck function in Equation (3), until the photodetector saturation level ($V_{MAX} = 10$ V) is reached or, more accurately, by replacing this value in the inverse Planck function—i.e., Equation (4). In a similar way, minimum measurable temperatures were estimated by replacing the noise level ($V_{noise} \approx 1$ mV) in the inverse Planck function. Table 2 shows minimum and maximum measurable temperatures.

Table 2. Minimum and maximum measurable temperatures.

λ_i [nm]	T_{MIN} [K]	T_{MAX} [K]
850	1260	4160
1050	1260	7470
1300	960	4740

4. Dynamic Tests

4.1. Test Rig

To demonstrate the speed of the instrument, dynamic tests were performed using theatrical flash charges [5] in the pyrotechnic facility at NPL (National Physical Laboratory). This consists of a vented enclosure where pyrotechnic charges, placed on a stage, are remotely triggered with a controller that is connected and synchronised with the instrument. The sensor is mounted such that its front end protrudes into the enclosure with its tip ~ 15 cm above and ~ 5 cm away from the centre of the charge. The optimum position of the sensor is based on experience from previous tests, when we also conducted absorption/transmission experiments, from which no optical transmission was observed during the explosion, thus suggesting that the fireball is opaque and supporting our blackbody assumption, and an initial absorption coefficient $\alpha_0 = 0.25$ cm $^{-1}$ was estimated at $\lambda \approx 850$ nm.

4.2. Test Method

Two sets of explosion tests were performed: a preliminary set of 3 tests with medium pyrotechnic charges and another set of 3 tests with large pyrotechnic charges. In all cases, the photodetector gain was set at $G = 30$ dB, as the instrument was calibrated only with this setting. Sampling rate and number

of samples were set, respectively, at $f = 50$ kHz and $N = 50,000$ (giving an acquisition time $t = N/f = 1$ s) for the first 4 tests and then at $f = 250$ kHz and $N = 25,000$ (giving an acquisition time $t = N/f = 0.1$ s) for the last 2 tests. Sampling rate f and number of samples N were initially chosen based on experience from previous explosion tests, to collect enough data at a high speed but without having to record excessive data. N and f were changed in the last two tests, based on observations from the previous test, again to avoid recording data where no signal was present, but also to capture finer details and test the maximum sampling speed.

4.3. Test Results

The preliminary set of tests with medium pyrotechnic charges (shown in Figure 10) demonstrated that $f = 50$ kHz was sufficient to measure the rapid temperature rise and decay and identify signal structure in between. Variability in temperature evolution was observed from test to test—this was to be expected as no two charges are the same. Nevertheless, there was a good correlation among all traces for a given test, although the temperature agreement was poor—in particular, the temperature estimated from the signal at $\lambda_3 = 1300$ nm was significantly lower than the other two, by up to ~ 600 K. This suggested that the effective emissivity at the longest wavelength was significantly less than unity—i.e., the blackbody condition necessary for successful thermometry is not met. On the contrary, the set of tests with large pyrotechnic charges shown in Figure 11 produced more consistent results and better agreement among temperatures measured at different wavelengths, meaning that the blackbody condition ($\varepsilon = 1$) is more closely met than with medium charges. In explosion tests with large charges, the maximum temperatures estimated at different wavelengths agree with each other within up to ~ 137 K or $\sim 4.5\%$.

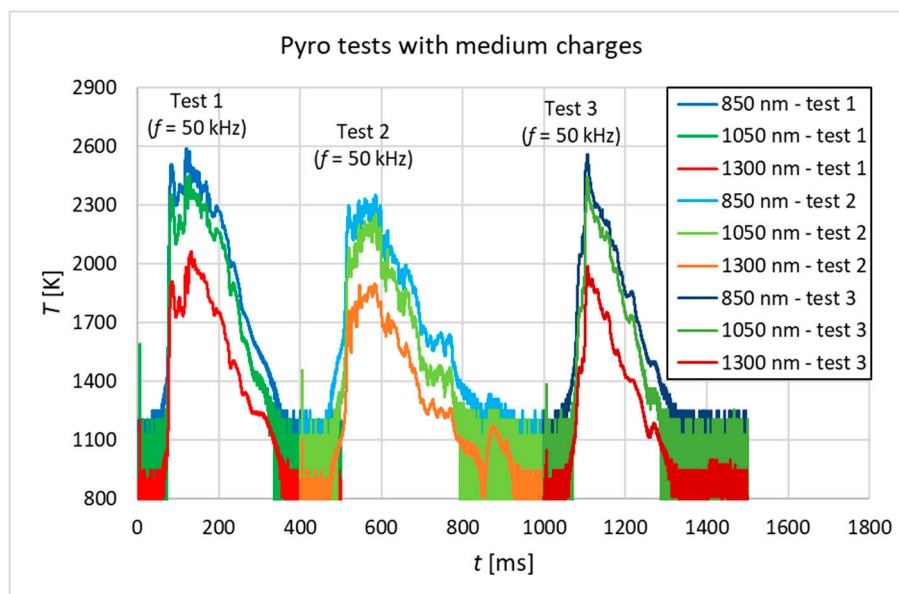


Figure 10. Time trend of temperatures for pyrotechnic tests with medium charges—temporal offset introduced for clarity.

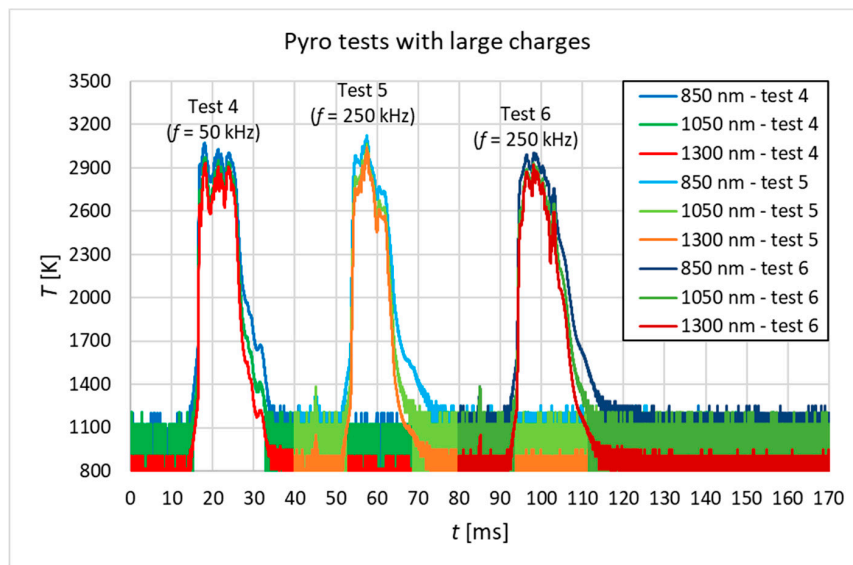


Figure 11. Time trend of temperatures for pyrotechnic tests with large charges—temporal offset introduced for clarity.

Figure 11 shows again that a sampling rate of $f = 50$ kHz was still fast enough to capture events from large charges, despite shorter pulse duration (<20 ms versus ~ 200 ms), sharper rise time (<1 ms versus ~ 10 ms) and faster decay times (~ 10 ms versus ~ 100 ms) than medium charges. The sampling rate was increased to $f = 250$ kHz in the last two trials to test the maximum sampling frequency allowed by the gain set in the photodetectors ($G = 30$ dB). A temperature rise of up to ~ 3.25 K/ μ s was estimated for explosions of large charges.

Figure 12 shows that large pyrotechnic charges produced not only more consistent results, but also higher peak temperatures than medium charges, by ~ 700 K. It is also worth observing that the temperature measured at $\lambda_1 = 850$ nm was always the highest, whereas the temperature measured at $\lambda_3 = 1300$ nm was always the lowest.

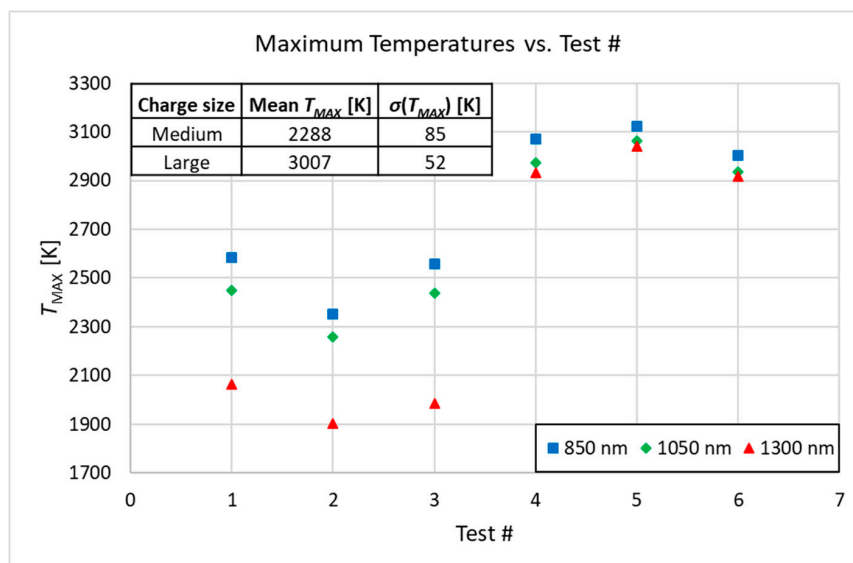


Figure 12. Plot of maximum temperatures versus test number. The inset on the upper left shows some statistics: $Mean T_{MAX}$ and $\sigma(T_{MAX})$ are, respectively, the average and the standard deviation of peak temperatures measured at different λ .

In any case, having calibrated our instrument with a blackbody cavity, it is possible to state that the fireball will have reached at least the highest measured temperature, regardless of the emissivity and of the blackbody assumption. In fact, if the blackbody assumption is made ($\varepsilon = 1$), but the true emissivity is $\varepsilon < 1$ and constant with wavelength (i.e., the fireball is not a blackbody, but a grey body), then the difference between the true temperature T and the measured temperature, also called colour temperature, T_c , can be written as:

$$\frac{1}{T} = \frac{1}{T_c} + \frac{\lambda}{c_2} \ln(\varepsilon)$$

From this expression, an error in emissivity of $\Delta\varepsilon$ will lead to an error in the inferred temperature:

$$\Delta T = -\frac{\lambda T^2}{c_2} \Delta\varepsilon$$

where: $\Delta T = T_c - T$ and $\Delta\varepsilon = 1 - \varepsilon$.

From the expression above, it is clear that the temperature error is temperature- and wavelength-dependent and that a grey body would not provide identical temperature readings at different wavelengths (as in the blackbody case), as shown also in Figure 13, where temperature error is plotted versus wavelength at three given emissivities at $T = 3000$ K, and in Figure 14, where temperature error is plotted versus true temperature at the three wavelengths used for $\varepsilon = 0.8$. It is worth observing that, for a given emissivity, the error is smaller for shorter wavelength, which agrees with the experimental findings (see Figure 12).

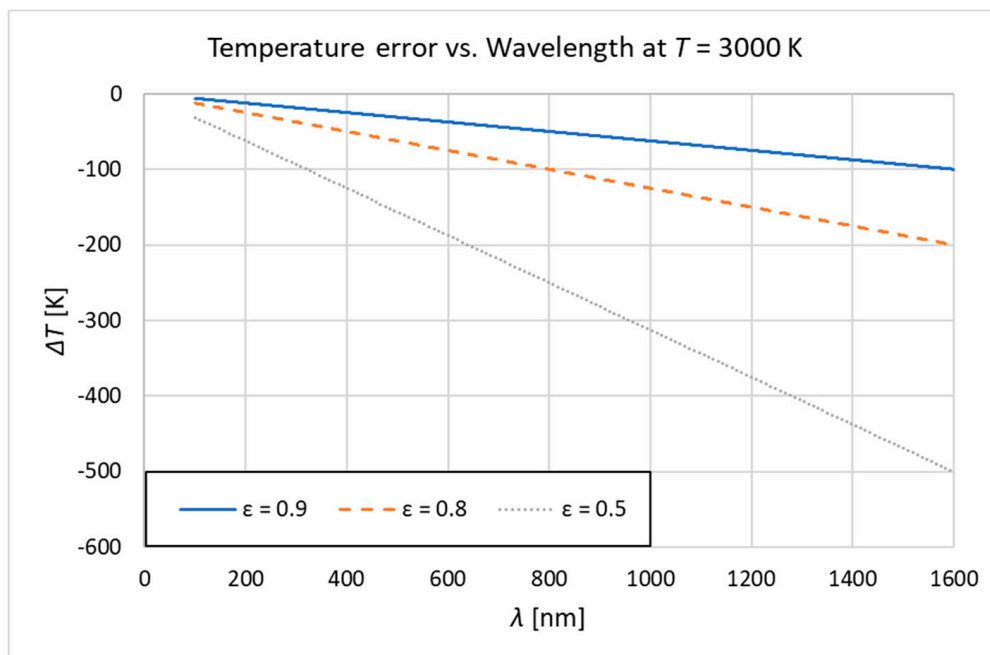


Figure 13. Plot of temperature error versus wavelength at $T = 3000$ K for different values of emissivity.

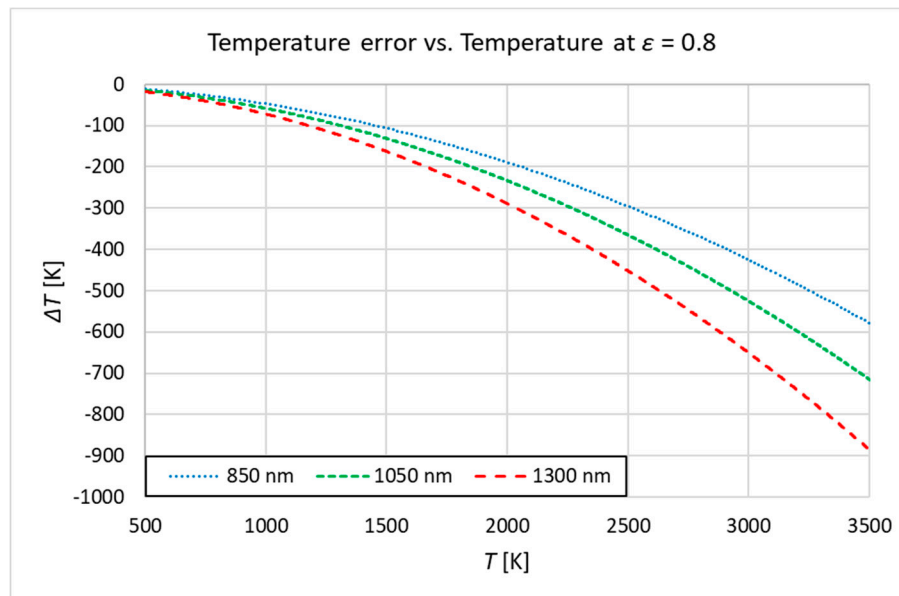


Figure 14. Plot of temperature error versus temperature for $\varepsilon = 0.8$ and for the three chosen wavelengths.

5. Conclusions

In summary, a novel ultra-high-speed combustion pyrometer, based on collection of thermal radiation via an optical fibre, was successfully designed, developed and tested. The instrument was traceably calibrated to the ITS-90 over the temperature range $T = (1073\text{--}2873)$ K with residuals $<1\%$. Dynamic tests with pyrotechnic charges demonstrated that the instrument can measure rapid (sub-ms) events, due to its high sampling rate (up to 250 kHz): a temperature rise of up to ~ 3.25 K/ μ s was estimated for explosions of large pyrotechnic charges. The accuracy of the temperature measurements can be assessed by considering the extent of agreement between readings at the three wavelengths—a self-diagnostic feature that is a critical strength of the technique. However, even when agreement between temperatures is poor, we can say, with a high level of confidence, that the fireball temperature is at least that reported by the reading at 850 nm. In future, the instrument will be tested in a maritime test engine.

Author Contributions: Conceptualization, G.S.; methodology, A.S. and G.S.; software, A.S., D.L. and G.S.; validation, A.S.; formal analysis, A.S.; investigation, A.S. and D.L.; resources, A.S., D.L. and G.S.; data curation, A.S.; writing—original draft preparation, A.S.; writing—review and editing, D.L. and G.S.; visualization, A.S.; supervision, G.S.; project administration, A.S. and G.S.; funding acquisition, G.S. All authors have read and agreed to the published version of the manuscript.

Funding: This work was funded through the European Metrology research Programme (EMRP) Project 17IND07 DynPT. The EMRP is jointly funded by EMRP participating countries within EURAMET and the European Union.

Conflicts of Interest: The authors declare no conflict of interest. The funders had no role in the design of the study; in the collection, analyses, or interpretation of data; in the writing of the manuscript, or in the decision to publish the results.

References

- Teichmann, R.; Wimmer, A.; Schwarz, C.; Winklhofer, E. Combustion Diagnostic. In *Combustion Engines Development—Mixture Formation, Combustion, Emissions and Simulation*; Merker, G.P., Schwarz, C., Teichmann, R., Eds.; Springer: Berlin/Heidelberg, Germany, 2012; p. 115.
- Saxholm, S.; Högström, R.; Sarraf, C.; Sutton, G.; Wynands, R.; Arrhen, F.; Jönsson, G.; Durgut, Y.; Peruzzi, A.; Fateev, A. Development of measurement and calibration techniques for dynamic pressures and temperatures (DynPT): Background and objectives of the 17IND07 DynPT project in the European Metrology Programme for Innovation and Research (EMPIR). *J. Phys. Conf. Ser.* **2018**, *1065*, 162015. [[CrossRef](#)]

3. Preston-Thomas, H. The International Temperature Scale of 1990 (ITS-90). *Metrologia* **1990**, *27*, 3–10. [[CrossRef](#)]
4. Saunders, P.; White, D.R. Physical basis of interpolation equations for radiation thermometry. *Metrologia* **2003**, *40*, 195–203. [[CrossRef](#)]
5. Safety Datasheet of LeMaitre Ltd. Theatrical Flashes. Available online: <https://www.lemaitreltd.com/products/pyrotechnics/pyroflash/theatrical-flashes-stars/theatrical-flashes/sds-flashes-robotics-spds/> (accessed on 22 November 2020).

Publisher’s Note: MDPI stays neutral with regard to jurisdictional claims in published maps and institutional affiliations.



© 2020 by the authors. Licensee MDPI, Basel, Switzerland. This article is an open access article distributed under the terms and conditions of the Creative Commons Attribution (CC BY-NC-ND) license (<http://creativecommons.org/licenses/by-nc-nd/4.0/>).